Coded Pulse Excitation for Ultrasonic Strain Imaging

Jie Liu and Michael F. Insana, *Member, IEEE*

***Abstract*—Decorrelation strain noise can be significantly reduced in low echo-signal-to-noise (eSNR) conditions using coded excitation. Large time-bandwidth-product (>30) pulses are transmitted into tissue mimicking phantoms with 2.5-mm diameter inclusions that mimic the elastic properties of breast lesions. We observed a 5–10 dB improvement in eSNR that led to a doubling of the depth of focus for strain images with no reduction of spatial resolution. In high eSNR conditions, coded excitation permits the use of higher carrier frequencies and shorter correlation windows to improve the attainable spatial resolution for strain relative to that obtained with conventional short pulses. This paper summarizes comparative studies of strain imaging in noise-limited conditions obtained by short pulses and four common aperiodic codes (chirp, Barker, suboptimal, and Golay) as a function of attenuation, eSNR and applied strain. Imaging performance is quantified using SNR for displacement (SNR_d), local modulation transfer function (LMTF), and contrast-to-noise ratio for strain (CNR_ϵ). We found that chirp and Golay codes are the most robust for imaging soft tissue deformation using matched filter decoding. Their superior performance is obtained by balancing the need for low-range lobes, large eSNR improvement, and short-code duration.**

I. Introduction

There is considerable recent interest in the use of compressible transmission codes for medical ultrasonic imaging. Under low echo-signal-to-noise-ratio (eSNR) conditions, temporally coded excitation pulses provide distinct advantages. For example, they have been shown to improve eSNR in vascular imaging with intravascular ultrasound (IVUS) arrays [1], in bone attenuation estimates [2], in bubble-preserving, nonlinear contrast imaging [3], in three-dimensional (3-D) imaging using parallel acquisition [4], and in very high frame rate 2-D acquisitions when combined with spatial encoding [5]. Coded excitation provides greater penetration by increasing the average power delivered to tissues without increasing peak power [6]–[8].

Our application is elasticity imaging. Specifically, the interest is strain estimation for breast cancer detection in which the visibility of small lesions is limited primarily by decorrelation noise. Low eSNR reduces the coherence between sequential echo frames acquired for correlation-based displacement estimates [9]. As a result large displacement errors are generated that appear in strain images as a high-intensity noise known as decorrelation noise. In this situation, longer correlation window lengths reduce decorrelation noise for small tissue deformations at the cost of slightly reduced axial resolution. Here we explore applications of coded pulse excitation methods to strain estimation in low eSNR conditions (<40 dB). The same methods may be applied in high eSNR situations to improve spatial resolution by allowing the use of higher carrier frequencies.

Coded excitation involves the transmission of long-duration pressure pulses with a time-bandwidth product (TBP) greater than 1. By coding the pulse on transmission, the received echo signals may be processed to compress (decode) the effective impulse response, and thus restore spatial resolution. If decoding is successful, eSNR is amplified by a factor equal to the TBP without compromising contrast or spatial resolution. If decoding is incomplete, the acoustic energy remains partially distributed spatially, producing range lobes that reduce B-mode image contrast. In strain imaging, range lobes increase decorrelation noise, particularly in high strain-contrast regions [10], thus negating the advantages of coded excitation. We have applied coded excitation methods to simulated and experimental phantom echo data to find which codes and associated parameters improve the quality of strain estimates.

O'Donnell [6] found that 15–20 dB improvements in eSNR are possible for typical B-mode imaging situations. The factors that must be considered when applying coded pulse excitation to B-mode imaging include eSNR, frequency-dependent absorption, clutter from range lobes, axial resolution, and frame rate (multipulse codes). In addition, we must add the effects of code distortion caused by the physical deformation of the scattering medium to consider applications in strain imaging. The goal is to translate improvements in eSNR into improvements in displacement and strain SNR while retaining acceptable levels of strain image contrast and spatial resolution.

II. Methods

Each step in the formation of a strain image is discussed below, from coded-pulse transmission through strain estimation. The entire process is summarized in Fig. 1.

Strain is estimated by comparing echo frames recorded before and after a deformation. The nth echo sample $g'_j[n]$ recorded in frame j arises from a one-dimensional (1-D)

Manuscript received January 28, 2004; accepted June 25, 2004. This work was supported in part by NIH R01 CA82497 and Siemens Medical Solutions, Inc. USA, Ultrasound Division.

The authors are with the Department of Biomedical Engineering, University of California Davis, Davis, CA (e-mail: jieliu@ucdavis.edu).

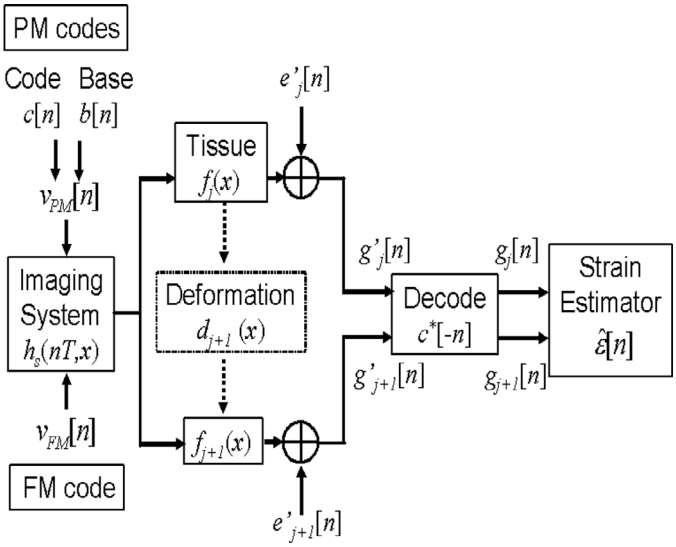

Fig. 1. Strain estimator using PM and FM coded pulse transmission. Conventional pulse-echo methods are obtained by setting $v[n] = \delta[n]$.

random scattering function $f_j(x)$ through the continuous-to-discrete integral transformation:

$$g'_j[n] = \int_{-\infty}^{\infty} dx\, h(nT, x) f_j(x) + e'_j[n], \qquad (1)$$

where $e'_j[n]$ is a sample of the signal independent noise vector and $h(nT, x)$ is the shift-varying impulse response of the system. Time $t = nT$ is sampled on the interval T with integer n. Arguments in brackets (parentheses) indicate functions of discrete (continuous) variables; f and e' are wide-sense stationary (WSS) random processes.

A. System Impulse Response

1. Binary PM sequences: $h(nT, x)$ for a phase-modulated (PM) sequence has three components. First, a code of length K bits is selected for properties related to orthogonality (matched filter decoding) or low noise amplification (inverse filter decoding) [11]. For example, a $K = 13$-bit Barker code can be written as the hexadecimal number "00CA". Converting to binary and then remapping $1 \rightarrow -1$ and $0 \rightarrow +1$, the code sequence is $\tilde{c}[k] = [1\,1\,1\,1\,1\,-1\,-1\,1\,1\,-1\,1\,-1\,1]$. It is expanded in time by the factor L to match the RF sampling rate using the expression [12]:

$$c[n] = \sum_{k=-\infty}^{\infty} \tilde{c}[k]\delta[n - kL],$$

where $\delta[n]$ is a Kronecker delta. Codes included in this study are listed in Table I.

The second component is an L-bit base sequence $b[n]$ [8]. Its convolution with c gives the transducer excitation voltage waveform for PM codes:

$$v_{PM}[n] = \sum_{k=-\infty}^{\infty} b[n - k]c[k] \triangleq \{b * c\}[n].$$

TABLE I
BINARY PM CODES USED IN THIS PAPER.

Code	Length (bit)	Hexadecimal
Barker	7	72
Barker	13	00CA
Suboptimal	32	FA6D48C7
Golay	8	12; 1D
Golay	32	121D12E2; 121DED1D

The form of the base sequence and its length determine the center frequency and bandwidth of v_{PM}. For example, our experimental conditions include $f_0 = 10$ MHz transducer resonant frequency, $\Delta f/f_0 = 0.6$ relative bandwidth, and $f_s = 40$ Msample/s sampling rate ($T = 25$ ns). The integer expansion factor is $L = f_s/\Delta f = 7$ and the base sequence is $b[n] = [1\,1\,-1\,-1\,1\,1\,-1]$. The period of the base-sequence square wave is $4T = 1/f_0 = 0.1$ μs. Also, it contains roughly three half cycles of the square wave, so the bandwidth is 57%. Although the duration of coded excitation voltage waveforms can be 5.58 μs (typical for $K = 32$-bit), the bandwidth is broad and consequently these pulses have large time-bandwidth products, TBP $= K$.

The third component is the pulse-echo impulse response of the ultrasonic system $h_s(nT, x)$, a function of space and time. The net impulse response is a convolution between the voltage waveform and the system impulse response:

$$h(nT, x) = \sum_{m=-\infty}^{\infty} v_{PM}[n - m]h_s(mT, x) = \{b * c * h_s\}(nT, x).$$

All three components of the linear system are assumed to be time invariant.

2. FM bursts: $h(nT, x)$ for a linear frequency-modulated (FM chirp) bursts [13] can be represented by two components as illustrated in Fig. 1. The chirp voltage is:

$$v_{FM}[n] = w[n] \exp\left(i2\pi\left(f_0 nT + \alpha(nT)^2\right)\right), \qquad (2)$$

where $\alpha = \Delta f/T_p$ is the frequency-ramp constant in MHz/μs; $w[n]$ is a Tukey window function [14]:

$$w[n] = \begin{cases} 0.5\left(1 + \cos\left(\pi \frac{n - N_p/4(1+\beta)}{N_p/2(1-\beta)}\right)\right) & \frac{N_p(1+\beta)}{4} \le \left|n - \frac{N_p}{2}\right| \le N_p, \\ 1 & 0 \le \left|n - \frac{N_p}{2}\right| \le \frac{N_p(1+\beta)}{4} \end{cases},$$

where $T_p = N_p T$ is the pulse duration and $\beta \in [0, 1]$, such that $\beta = 0$ is a rectangular window, and $\beta = 1$ is a Hanning window. T_p and β are selected to minimize range-lobe amplitudes (-13 dB when $\beta = 0$ [15]) without excessively broadening the main lobe. The ultrasonic system $h_s(nT, x)$ is the same as for the PM codes.

B. Echo Signals

The jth coded echo frame $g'_j[n]$ is the reference or precompression frame [see (1)], $g'_{j+1}[n]$ is the postcompression frame, and both are nonstationary random processes. We assume all tissue motion occurs between frame acquisitions. Echo frames can be "coherent" when the scattering functions for g'_j and g'_{j+1} are related by a material description of continuum motion (one-to-one mapping of scatterers) [16]:

$$f_{j+1}(x) = f_j(x + d(x)),$$

where $d(x)$ describes spatially varying scatterer displacements resulting from an applied deformation force [17].

C. Pulse Compression

Appropriate filtering of the received echo signals minimizes the correlation length of g'_j if the code sequence is well designed. We chose the matched filtering approach [13], whereby, for PM codes, g'_j are convolved with the matched filter $c^*[-n]$ to produce a decoded echo signal g_j having a TBP that is approximately one:

$$\begin{aligned} g_j[n] &= \hat{\phi}_{cg'}[n] \triangleq \sum_{m=-\infty}^{\infty} c^*[m-n] g'_j[m] \\ &= \left[\sum_{\ell=-\infty}^{\infty} \phi_{cc}[n-\ell] \int_{-\infty}^{\infty} dx\, h_{sb}(\ell T, x) f_j(x) \right] + e_j[n], \end{aligned} \quad (3)$$

where $h_{sb}[n] \triangleq (h_s * b)[n]$, $\phi_{xy} = \mathcal{E}\left\{\hat{\phi}_{xy}\right\}$ is the correlation function between sequences x and y, and $\mathcal{E}\{\cdot\}$ is the expectation operator. $e_j[n] = \hat{\phi}_{ce'}[n]$ is a filtered noise realization.

A code sequence is optimal when the range lobes are the smallest possible [13]. For example, the PM Barker code is optimal because $\phi_{cc}[n]/\phi_{cc}[0] \simeq 1/K$ for $n \neq 0$. Unfortunately, the maximum Barker sequence is 13 bits. To achieve high eSNR, longer, suboptimal codes suggested by others [11] also were examined. Optimal codes with long sequences approximate the result $\phi_{cc}[n] \simeq K\delta[n]$, so that (3) reduces to:

$$\begin{aligned} g_j[n] &\simeq K \int_{-\infty}^{\infty} dx\, h_{sb}(nT, x) f_j(x) + e_j[n] \\ &= s_j[n] + e_j[n]. \end{aligned} \quad (4)$$

For Golay codes, $K \to 2K$. Scatterer motion, attenuation, and other common phenomena distort echo signals and thus increase range lobes often with little effect on the main lobe. In these situations, (3) rather than (4) more accurately represents the filtered echo frames g_j and g_{j+1}. Although (3) and (4) apply to PM codes, comparable results can be obtained for FM codes.

D. Strain Estimator

Decoded echo frames g_j and g_{j+1} are segmented and cross correlated to estimate local displacements using methods described elsewhere [9]. Phantom data were companded in 2-D prior to 1-D cross correlation to minimize decorrelation. Companding was not applied while estimating displacements in 1-D echo simulations. And, longitudinal strain estimates $\hat{\epsilon}[n]$ are computed from the spatial derivative of displacement along the direction of the beam axis. In practice, we apply a finite impulse response (FIR) differentiation filter h_d [12] to displacement estimates $\hat{d}[n] : \hat{\epsilon}[n] = \{h_d * \hat{d}\}[n]$.

E. Quality Metrics

Coded excitation was adapted to strain imaging by selecting code parameters that optimized the quality metrics described below.

1. eSNR: Pulse compression improves eSNR by increasing the echo signal energy more than the noise energy. To quantify the change in eSNR for our shift-varying system, we use (4) to find:

$$\begin{aligned} \mathrm{eSNR}[n] &= 10 \log \left(\frac{\phi_{ss}[0,n]}{\phi_{ee}[n]} \right) \\ &= 10 \log \left(\frac{\mathcal{E}\{|K \int_{-\infty}^{\infty} dx\, h_{sb}(nT,x) f_j(x)|^2\}}{\mathcal{E}\{|e[n]|^2\}} \right) \\ &= 10 \log \left(\frac{K^2 \sigma_f^2}{K \sigma_{e'}^2} \int_{-\infty}^{\infty} dx\, h_{sb}^2(nT,x) \right) \\ &= 10 \log K + \mathrm{eSNR}'[n], \end{aligned} \quad (5)$$

where σ_f^2 and $\sigma_{e'}^2$ are the object and noise variances and eSNR$'$ is the echo-signal-to-noise ratio for the conventional, short-duration pulse assuming no attenuation. The last form of (5) shows that eSNR for coded excitation is nominally larger than eSNR$'$ by the amount $10 \log K = 10 \log$ TBP.

2. LMTF: Local modulation transfer function (LMTF) is the normalized Fourier transform of the corresponding local impulse response (LIR). The LMTF is adopted to quantitatively evaluate the axial resolution of ultrasonic strain imaging. The base sequence $b(t)$ was selected to match the transducer bandwidth in order to maximize the acoustic power given the applied electrical power. As a result, we maximized eSNR at the cost of lengthening the compressed pulse, $h_{sb}[n] = (h_s * b)[n]$. In B-mode imaging, longer pulses translate directly into a loss of axial resolution. However, in strain imaging, the effect on axial resolution is not as obvious. The correlation window and pulse lengths both factor into the determination of axial resolution. In noise-limited strain estimation, the correlation window is set several times longer than the axial pulse dimension to suppress the effects of echo noise. The increased eSNR with coded excitation permit use of shorter

correlation windows, which could lead to comparable or superior axial resolution for strain despite a longer pulse length.

To test these ideas, we simulated nonstationary echo signals that enabled measurement of the LIR for strain estimates. The LIR is the output of the strain estimator $\mathrm{LIR}(nT, x_0) = \hat{\epsilon}[n]$ for a strain impulse input, i.e., $\epsilon(x) \propto \delta(x - x_0)$. Axial resolution for different pulses was compared using the normalized Fourier transform of the corresponding LIR—LMTF—via methods described previously [17]:

$$\mathrm{LMTF}_{x_0}[k] = \frac{\left|\sum_{n=1}^{N} \mathcal{E}\left\{\hat{\epsilon}\left(nT, x_0\right)\right\} e^{-i2\pi kn/N}\right|}{\sum_{n=1}^{N} \mathcal{E}\left\{\hat{\epsilon}\left(nT, x_0\right)\right\}}, \tag{6}$$

where N is the number of strain estimates in LIR. The shift variant system response means that LIR and LMTF vary with x_0.

3. SNR_d: The SNR_d estimates SNR_d [18] is found by applying a known input displacement $d(x)$ into our estimator and measuring the output $\hat{d}[n]$. For uniaxial compression applied to a homogeneous medium along the sound beam axis, the input displacement increases linearly with range. The figure of merit:

$$\mathrm{SNR}_d = 10 \log\left(\rho_{\hat{d}d}^2 / \left(1 - \rho_{\hat{d}d}^2\right)\right), \tag{7}$$

where:

$$\rho_{\hat{d}d}^2 = \frac{1}{N} \sum_{n=1}^{N} \frac{\phi_{\hat{d}d}^2[0, n]}{\phi_{dd}[0, n]\phi_{\hat{d}\hat{d}}[0, n]},$$

reaches its maximum value of one when the input and estimates are identical; $\hat{d}$ are computed from nonstationary echo data. Although the corresponding correlation coefficients can vary significantly with depth, the simple uniaxial deformation produced mean and variance measurements that did not vary significantly. Consequently, values were averaged as shown. The SNR_d is an appropriate measure for results obtained from 1-D echo simulations.

4. CNR_ϵ: To include effects that alter lesion contrast or any 2-D correlations that may exist among strain estimates, we adopted the contrast-to-noise ratio (CNR) to evaluate applications of coded excitation to strain images. Let $\bar{\hat{\epsilon}}_t$ and $\bar{\hat{\epsilon}}_b$ be the mean strains inside a lesion target and in the surrounding background, respectively. Also let var_t and var_b be the sample variances for the corresponding regions. Then:

$$\mathrm{CNR}_\epsilon = \frac{\bar{\hat{\epsilon}}_b - \bar{\hat{\epsilon}}_t}{\sqrt{\left(\mathrm{var}_b + \mathrm{var}_t\right)/2}}. \tag{8}$$

III. 1-D Simulations and Measurements

A. Echo Simulations

Object scatterers f_j are simulated numerically in 1-D using Monte Carlo methods [17]. The $h(nT, x)$ is modeled as a shift-varying pulse with center frequency 10 MHz, fractional bandwidth 0.6, and frequency-dependent attenuation. The pulse lengths of the short pulse, chirp with Tukey-window apodization, 32-bit Golay code, and 32-bit suboptimal code at 60% bandwidth are 0.077 mm, 4.9 mm, 4.3 mm, and 4.3 mm, respectively. The total energy transmitted is the same for all coding sequences. Each data point presented is comprised of measurements from 100 independent echo waveform pairs. Each pair is individually processed to estimate displacement and strain then averaged.

Two 1-D software phantoms were used to simulate echo signals from deformed media with different strain patterns. One provided a homogeneous strain along a 5-cm depth to study SNR_d in the ranges of $\mathrm{eSNR}' = 10$ to 60 dB, attenuation coefficient slope = 0.1 to 0.9 cm/dB/MHz, and applied strain 0.1% to 1%. The eSNR' is measured at the focal length of the aperture with no medium attenuation. In situations in which the attenuation slope is 0.6 dB/cm/MHz, eSNR' for our broadband system is reduced approximately 10 dB. The second software phantom provides an impulse strain (step displacement). This phantom is used to investigate the effects of the net impulse response on axial resolution.

B. Echo Simulation Results

Fig. 2(a) shows SNR_d for four different pulses as a function of eSNR' using the homogeneous software phantom. Other parameters are held constant. As expected, SNR_d increases with eSNR'. Coded pulses provide the greatest improvement over the short pulse at low eSNR'. The chirp and Golay pulse performances are nearly equal.

We fixed eSNR' at 40 dB then studied the effects of increasing the slope of the frequency-dependent attenuation coefficient using the homogeneous software phantom. Results are summarized in Fig. 2(b). The SNR_d values fall with increasing attenuation slope for all pulses, and the decline is much greater for the short pulse. Our simulation verified that coded pulse excitation (especially for chirp and Golay) significantly reduces strain noise in highly absorbing tissues.

Fig. 3(a) shows SNR_d for all pulses as a function of applied strain using the homogeneous phantom. Values were found to decrease with compressive strain. For small deformation, SNR_d was greater for the chirp and Golay pulses than the short pulse. For deformations greater than 0.7%, SNR_d for the chirp and Golay pulse are about 2 dB less than the short pulse.

As demonstrated in Figs. 2 and 3(a), chirp and Golay pulses have similar performances for SNR_d, but the suboptimal coded pulse is consistently inferior.

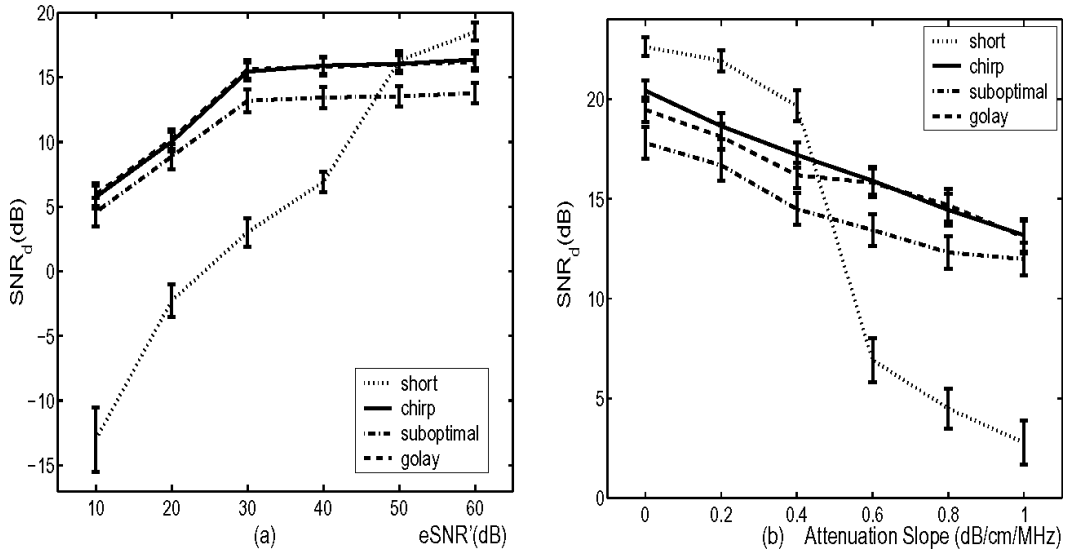

Fig. 2. (a) SNR_d for short pulse (dotted line), chirp pulse (solid line), 32-bit suboptimal code (dashdot line), and 32-bit Golay code (dashed line) are shown as a function of eSNR′. Attenuation coefficient slope is 0.6 dB/cm/MHz. (b) SNR_d for all pulses are shown as a function of attenuation coefficient slope. eSNR′ is 40 dB. The correlation window length was 1.23 mm, and the applied strain was 0.5% for all measurements.

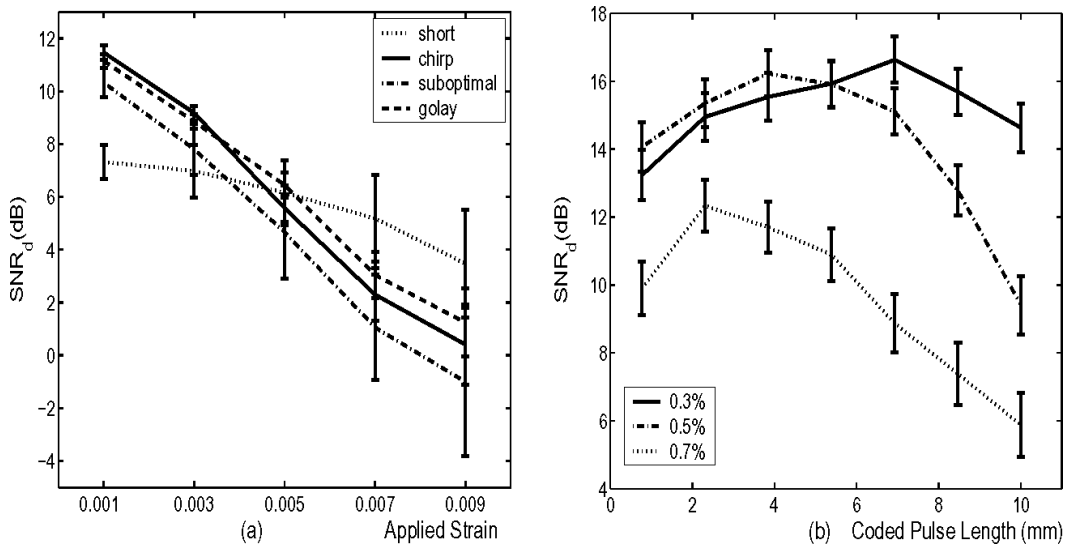

Fig. 3. (a) SNR_d for all pulses are shown as a function of applied strain. The correlation window length is 0.62 mm. (b) SNR_d for chirp pulse as a function of pulse length under applied strain 0.3%, 0.5%, and 0.7%, respectively. The correlation window length is 1.23 mm. The attenuation coefficient slope, 0.6 dB/cm/MHz, and eSNR′, 40 dB, are fixed.

Longer coded pulses, for example, 3.85 mm for 0.5% applied strain, have greater eSNR but their propagation through deformed media increases displacement noise because of the range lobes generated by incomplete pulse compression. Fig. 3(b) shows there is an optimal coded pulse length unique to the strain estimation conditions.

Because the greatest relative improvements in SNR_d for coded pulses occur at the smallest deformation, Fig. 3, it is reasonable to use multicompression methods [19]. Fig. 4 demonstrates SNR_d for the chirp as a function of pulse length using both single compression (0.3% and 0.6% applied strains) and multicompression ($2\times0.3\%$ strain) techniques. The SNR_d for the 7-mm-long chirp is nearly 4 dB greater for the $2 \times 0.3\%$ strain experiment than for the single 0.6% applied strain experiment.

Fig. 5(a) shows the LMTF curves for each pulse type when the correlation window length (0.077 mm) is shorter than all of the compressed pulse lengths (0.17 mm for the short pulse). For these curves, we studied the strain impulse software phantom. These LMTF curves define the upper limit of axial resolution because pulse length is the limiting factor [17]. Fig. 5(b) shows the LIR when the correlation window is longer than transducer pulse for the short and chirp pulses. The width of the main lobe shows the attainable resolution determined by the correlation window [17]. Fig. 5(a) predicts a small degradation in

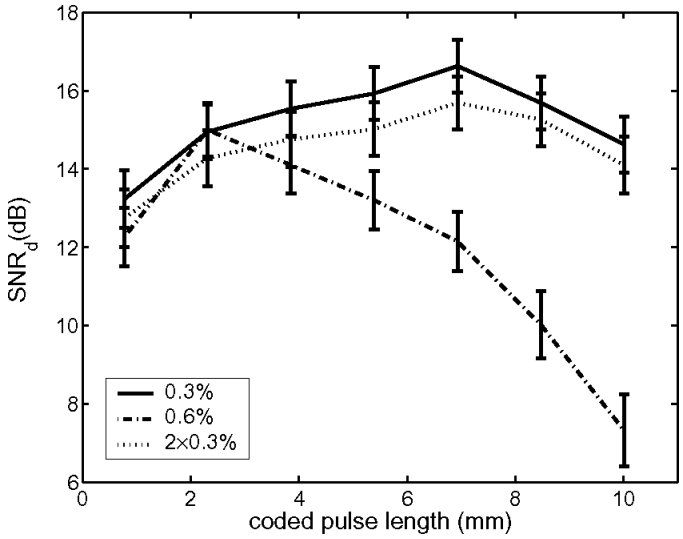

Fig. 4. SNR_d for chirp pulses as a function of pulse length under applied strains 0.3%, 0.6%, and $2 \times 0.3\%$ (multicompression), respectively. The correlation window length is 1.23 mm, $eSNR' = 40$ dB, and attenuation coefficient = 0.6 dB/cm/MHz are fixed.

upper bound resolution when coded excitation is applied. However, Fig. 5(b) shows coded excitation has lower strain noise under the same attainable resolution. Therefore, the increased SNR_d with coded pulse excitation permits use of shorter correlation windows and higher frequencies that enhance displacement and strain axial resolution. Fig. 6 shows SNR_d for the short and chirp pulses as a function of correlation window length (attainable resolution) using the homogeneous phantom. For example, $SNR_d = 20$ dB with a short pulse when the correlation window is 3.1 mm. However, we can obtain the same SNR_d using a chirp pulse with a 1.75-mm correlation window. Consequently, the relative spatial resolution for strain can be increased using coded excitation in low eSNR conditions.

IV. Phantom Measurements

A. The Experiment

We developed an ultrasonic strain imaging system [20] specifically for imaging tumors in small animals. An 8-ring, 30-mm diameter, f/1.5, spherically focused annular array was built to generate 10 MHz pulses with 60% bandwidth [21]. This transducer dynamically focuses on receive without aperture growth. Echoes are recorded with a sampling rate of 62.5 MHz while the transducer is mechanically scanned by a linear positioner under microprocessor control. The −6 dB depth of focus (DOF) for B-mode imaging is extended from 2.4 mm to just 3.2 mm after dynamic focusing. Therefore, the eSNR remained insufficient for strain imaging over a 10-mm depth near the focal length because of significant decorrelation errors from low eSNR.

We applied chirp and 13-bit Barker pulses designed to increase eSNR and allow decorrelation-free strain imaging over a 10-mm DOF. The lengths of the short, chirp (Tukey apodized), and Barker pulses were 0.217 mm (TBP $\simeq$ 1), 2.65 mm, and 2.17 mm (TBP $\simeq$ 10), respectively. For all sequences, the peak-to-peak excitation voltages (V_{pp} = 200v) and bandwidths were kept constant. The transmitted energy was held constant for all coded sequences. Consequently, the expected increase in eSNR was 10 dB. We measured an increase in the −6 dB DOF from 3.2 mm to 7 mm.

TABLE II
Experimental System −6 dB Resolution (mm).

Resolution	Short	Chirp	Barker
Axial	0.150	0.230	0.240
Lateral	0.226	0.226	0.220

A 35 mm × 10 mm graphite/agar phantom having acoustic properties similar to breast tissue was built for strain imaging. Measured attenuation is 5.4 dB/cm at 10 MHz. Three hard inclusions with diameter 2.5 mm were embedded at 2-mm, 5-mm, and 8-mm depths. The transmit focal zone is centered on the 5-mm deep inclusion.

This lesion-mimicking phantom can be used to study lesion visibility via CNR_ϵ. The estimate of the ratio of the elastic modulii of the background and inclusions is about 5 6. All processing was performed off-line on Pentium computers. When phantom strain images are computed, 2-D companding techniques [9] are applied to reduce out-of-plane motion and the amount of strain between g_1 and g_2 before cross correlation. Thus, the residual strain detected by the correlation estimator is less than 1%.

B. Experiment Results

We measured 2-D spatial sensitivity function (SSF) [22] for the short, chirp, and Barker pulses along the lateral (x) and axial (z) directions by scanning a point reflector in two different ways. First, we scanned the point reflector by moving the transducer on a fine mesh and recorded the peak pulse amplitude. The results are the SSF shown in Fig. 7. Penetration is greatly extended by coded excitation with some increase in range and side lobes.

The second measurement fixes the reflector in space at the focal length (45 mm) and records the echo amplitude as a function of time (axially) and space (laterally). Axial point spread function (PSF) and lateral SSF functions for short, chirp, and Barker pulses are demonstrated in Fig. 8 and Table II. Long pulse excitation degrades B-mode axial resolution due to blurring by the base sequence as predicted by simulation results, Fig. 5(a). Lateral resolution is determined by the product of wavelength and f-number, $\lambda \times f/\mathrm{No} = 0.148 \times 1.5 = 0.22$ mm, which is unaffected by the applied voltage, Fig. 8(b). Range lobes for the 13-bit Barker code are −22 dB lower than the main lobe peak in the axial direction, Fig. 8(a), and −6 dB lower in lateral direction.

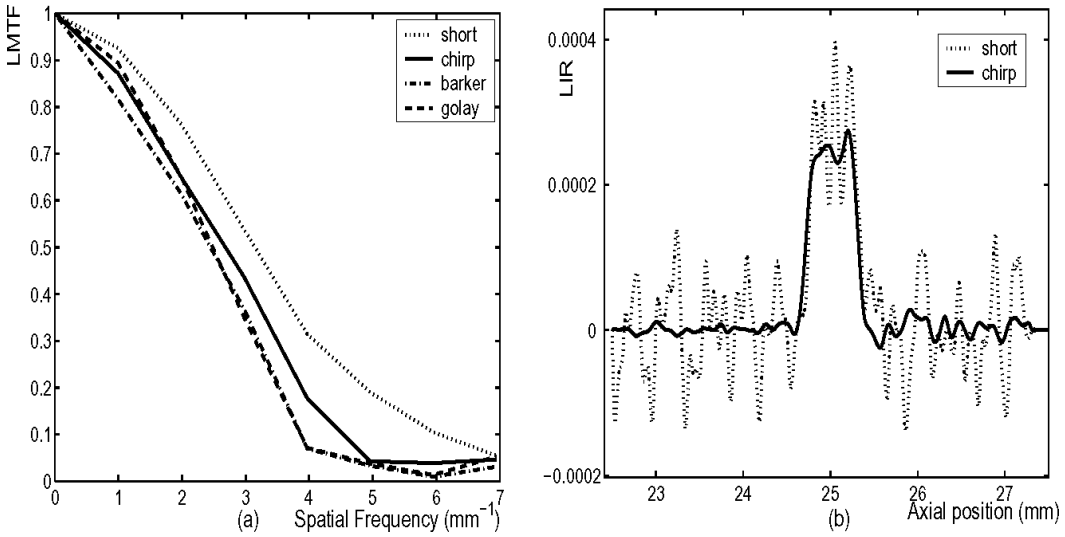

Fig. 5. (a) LMTF curves for short pulse, chirp pulse, 7-bit Barker code, and 8-bit Golay code. The correlation window length is 0.077 mm. eSNR′ = 1000 dB. Applied strain is 1%. (b) LIR for short pulse and chirp pulse under same attainable resolution. The correlation window length is 0.62 mm, eSNR′ = 40 dB, and applied strain is 1%.

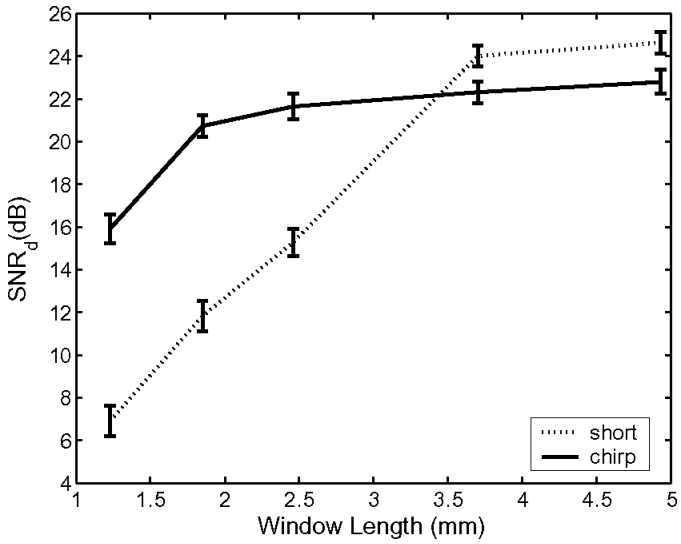

Fig. 6. SNR$_d$ for short and chirp pulse as a function of window length. eSNR′ = 40 dB, attenuation coefficient 0.6 dB/cm/MHz, and 0.5% applied strain are fixed.

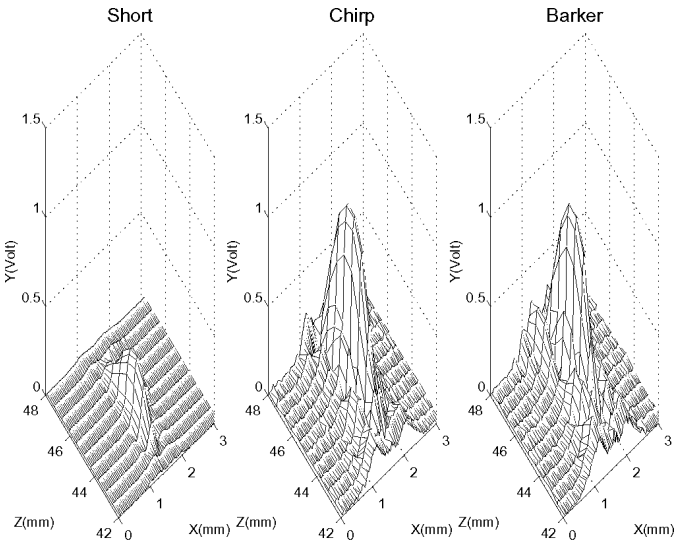

Fig. 7. Measured 2-D SSF for short, chirp, and Barker sequences.

Fig. 9 shows strain images of the lesion phantom for applied strains of 1%, 2%, and 3%, using short, chirp, and Barker pulses, respectively. Measured CNR$_\epsilon$ results from data in Fig. 9 are listed in Table III. Square boxes in Fig. 9 indicate regions from which CNR$_\epsilon$ in Table III are computed. The peak eSNR′ measured for our laboratory system is a meager 30 dB for the lesion phantom. Images in Fig. 9 are displayed with the same gray scale to show how greater phantom compression increases lesion contrast and decorrelation noise, particularly for the short and Barker pulses. Comparing the strain images, it is clear that the chirp pulse can successfully suppress decorrelation strain noise under noise-limited condition. Although the Barker pulse improves eSNR, its range side lobes induce decorrelation noise at larger deformations. Its performance is equivalent to the short pulse as predicted by the simulation results, Fig. 2(a).

TABLE III
CNR$_\epsilon$ Measured for Lesion Phantom in Fig. 9.

Strain	Short	Chirp	Barker
1%	1.47	2.51	1.53
2%	0.05	1.58	0.03
3%	0.04	1.26	0.02

Fig. 10 compares the strain images of a lesion phantom with 1% applied strain for short pulse and chirp pulse using 1.58-mm and 0.79-mm correlation window lengths. Measured CNR$_\epsilon$ results are shown in Table IV. Chirp pulses provide greater CNR$_\epsilon$ than short pulses with

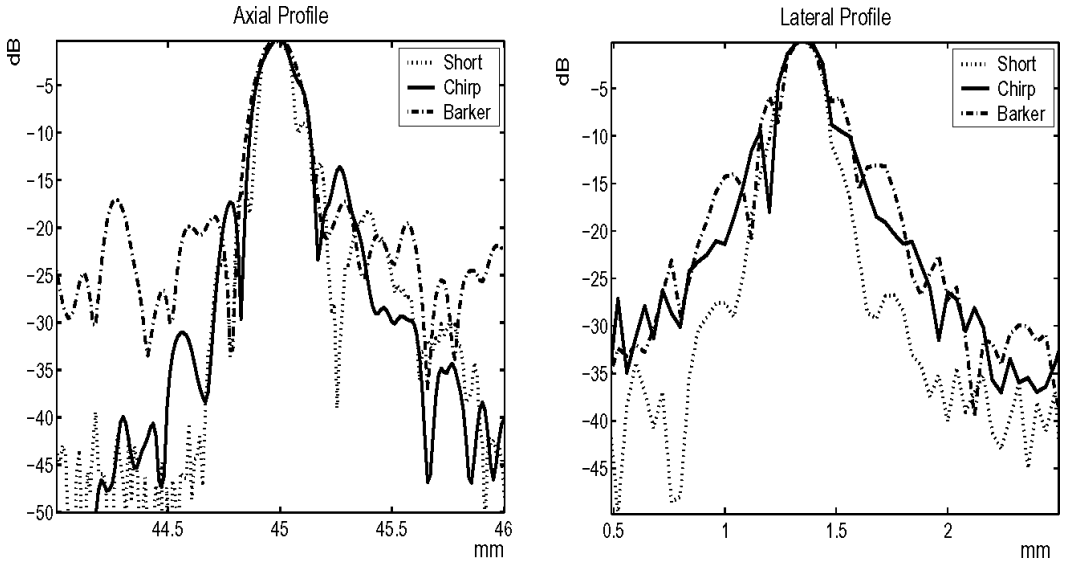

Fig. 8. Measured axial PSF (a) and lateral SSF (b) for short, chirp, and Barker pulses at focal depth.

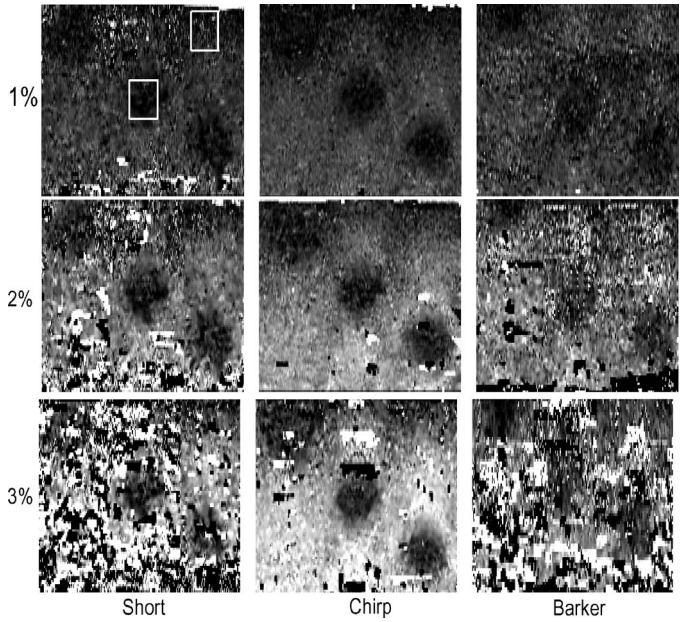

Fig. 9. Strain images of a lesion phantom with 1%, 2%, and 3% strain applied from top. The excitation pulses are the short pulse (left column), chirp (middle column), and Barker code (right column). The correlation window is fixed at 1.58 mm. Each image size is 13.3 mm × 10.7 mm. Boxes indicate regions from which strain contrast to noise ratios in Table III are computed.

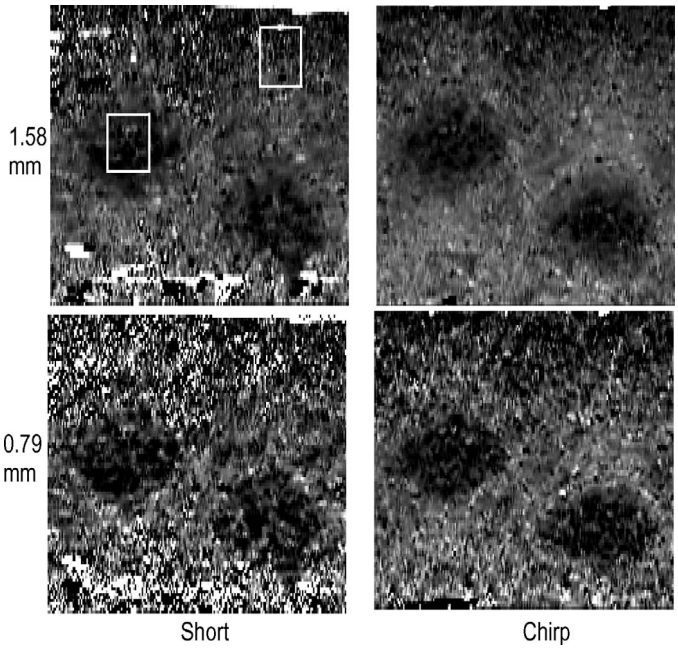

Fig. 10. Strain images of a lesion phantom with 1% applied strain. The excitation pulses are short (left) and chirp (right). The correlation windows are 1.58 mm and 0.79 mm from top to bottom, respectively. Each image size is 8.8 mm × 10.7 mm.

TABLE IV
CNR_ϵ MEASURED FOR LESION PHANTOM IN FIG. 10.

Window length	Short	Chirp
1.58 mm	1.47	2.51
0.79 mm	0.23	1.41

the same correlation window length. From Table IV, the chirp pulse has almost the equal CNR_ϵ as the short pulse but with half the window length. Recall that the window length determines the attainable axial resolution for strain imaging. Therefore, to keep the same lesion detectability, the chirp pulse requires a shorter correlation window.

V. Discussion and Conclusions

This paper describes a method for adapting common coded excitation pulses to strain imaging. It also presents

a preliminary study based on simulated echo data using parameters of the Siemens Antares system as well as phantom experiments using a laboratory system. We compared the performance of conventional short pulse and coded pulse excitations under the operating conditions of breast imaging. The measured results demonstrate that it is feasible to apply coded excitation technique for ultrasonic strain imaging. Many operating factors (such as electronic noise, ultrasonic attenuation, and applied deformation) will affect strain image quality. To maximize the performance, the coding parameters must be carefully chosen. To obtain the highest performance, the choice of pulse and associated parameters is application dependent.

Fig. 2(a) shows that, when $\text{eSNR}' > 50$ dB, SNR_d is greatest for the short pulse. When $\text{eSNR}' < 50$ dB, the chirp and Golay pulses yield the lowest strain noise. It suggests that to obtain a low-noise strain image along an extended field of view, one should apply short pulses in high eSNR regions (for example, near the focus), and coded long pulses should be applied in low eSNR regions (e.g., in which there is acoustic shadowing or deep in the body).

Fig. 2(b) predicts that coded excitation significantly reduces strain noise in highly absorbing tissue. The estimated attenuation for fibroglandular tissue in breast is 22.8 dB/cm for a 10 MHz transducer [23]. The slope of ultrasonic attenuation for some carcinomas is about 0.08–1.6 dB/cm/MHz [24]. Coded excitation has great potential for reducing strain noise in absorbing media such as breast tissue.

The greatest improvement in SNR_d with coded pulses is obtained at the smallest applied deformations, e.g., Fig. 3(a). Also small deformations allow use of longer code [see Fig. 3(b)]. Both of these results suggest that multicompression methods combined with coded excitation will be very effective, e.g., see Fig. 4.

A previous study [17] showed that B-mode axial resolution determines the upper bound for strain axial resolution. For our approach to coded excitation, the upper limit on axial resolution is further limited by the base sequence as given by h_{sb} and shown in Fig. 5(a), Fig. 8(a), and Table II results. Using the spatial frequency at LMTF = 0.1 as the axial resolution limit [17], predictions in Fig. 5(a) agree with the measurements in Fig. 8(a). However, in common practice, the duration of the correlation window determines attainable axial resolution. Fig. 5(b), Fig. 10, and Table IV demonstrate the improvement in SNR_d using coded pulses can be converted to improvement in attainable axial resolution. The lateral resolution in strain imaging is on the same order as in B-mode [25]. Because the coding and decoding procedure have no effect on transducer aperture size, lateral resolution remains unchanged by the excitation [see Fig. 8(b)].

Our comparative study of the performances of chirp, Barker, suboptimal, and Golay codes shows that designing sequences robust to deformations is challenging for strain imaging. The simulations predict chirp and Golay code have better performance than suboptimal and Barker code. Experiments verify the predictions that it is easier to detect small lesions using chirp pulse than Barker code under noise-limited condition. Due to our limited hardware, Golay code excitation was not tested during experiments. However, because the experimental results using chirp and Barker codes agree with predictions, we expect the Golay code predictions to be verified also. A variety of other codes available for ultrasonic imaging will be studied in our future work, such as m-sequence and Huffman sequence [15].

Matched filters were used to decode echoes. Although this approach maximizes eSNR, it introduces range lobes. As the simulations and experiments showed, range lobes act to decorrelate echoes in deformed media. For Barker and suboptimal codes, the level of the range lobe is often too high for strain imaging, roughly −20 dB below that of the main lobe.

Echoes also may be decoded by inverse compression filters or an adaptive combination of matched and inverse filtering given by the Wiener filter [7]. For a general compression filter h_c, the echo signal in (3) is written as:

$$g_j[n] = \sum_{m=-\infty}^{\infty} h_c[m-n] g_j'[m],$$

where the system response of the filter is:

$$H_c[k] = \frac{C^*[k]}{|C[k]|^2 + \mathcal{E}\left\{|E'[k]l^2\right\} / \mathcal{E}\left\{|S'[k]|^2\right\}}, \qquad (9)$$

and $C^*[k]$, $S'[k]$, and $E'[k]$ are the discrete Fourier transforms of $c^*[-n]$, $s'[n]$, and $e'[n]$, respectively. The compression filter H_c is approximately proportional to the match filter $C^*[k]$ when the noise power is relatively large and the inverse filter $C^{-1}[k]$ with the noise power is relatively small. We focused the matched filter over the inverse filter because of its greater stability in noisy conditions, its ease of use, and its ability to achieve the largest eSNR regardless of the code [8]. The goal is to design $|C[k]|$ to be constant over the transducer bandwidth. In that case the matched and inverse filters perform equivalently within a scale factor.

References

[1] Y. Wang, K. Metzger, D. N. Stephens, G. Williams, S. Brownlie, and M. O'Donnell, "Coded excitation with spectrum inversion (CEXSI) for ultrasound array imaging," *IEEE Trans. Ultrason., Ferroelect., Freq. Contr.*, vol. 50, pp. 805–823, 2003.

[2] A. Nowicki, J. Litniewski, W. Secomski, P. A. Lewin, and I. Trots, "Estimation of ultrasonic attenuation in a bone using coded excitation," *Ultrasonics*, vol. 41, pp. 615–621, 2003.

[3] J. M. G. Borsboom, C. T. Chin, and N. de Jong, "Nonlinear coded excitation method for ultrasound contrast imaging," *Ultrasound Med. Biol.*, vol. 29, pp. 277–284, 2003.

[4] J. Shen and E. S. Ebbini, "Filter-based coded-excitation system for high-speed ultrasonic imaging," *IEEE Trans. Med. Imag.*, vol. 17, pp. 923–934, 1998.

[5] T. Misaridis and J. A. Jensen, "Space-time encoding for high frame rate ultrasound imaging," *Ultrasonics*, vol. 40, pp. 593–597, 2002.

[6] M. O'Donnell, "Coded excitation systems for improving the penetration of real-time phased-array imaging systems," *IEEE*

Trans. Ultrason., Ferroelect., Freq. Contr., vol. 39, pp. 341–351, 1992.
[7] B. Haider, P. A. Lewin, and K. E. Thomenius, "Pulse elongation and deconvolution filtering for medical ultrasonic imaging," *IEEE Trans. Ultrason., Ferroelect., Freq. Contr.*, vol. 45, pp. 98–113, 1998.
[8] R. Y. Chiao and X. Hao, "Coded excitation for diagnostic ultrasound: A system developer's perspective," in *Proc. IEEE Ultrason. Symp.*, 2003, pp. 437–448.
[9] R. Y. Chiao and X. Hao, "2-D companding for noise reduction in strain imaging," *IEEE Trans. Ultrason., Ferroelect., Freq. Contr.*, vol. 45, pp. 179–191, 1998.
[10] P. Chaturvedi, M. F. Insana, and T. Hall, "Testing the limitations of 2-D local companding in strain imaging using phantoms," *IEEE Trans. Ultrason., Ferroelect., Freq. Contr.*, vol. 45, pp. 1022–1031, 1998.
[11] J. Ruprecht and M. Ropf, "On the search for good aperiodic binary invertable sequences," *IEEE Trans. Inform. Theory*, vol. 42, pp. 1604–1612, 1996.
[12] A. V. Oppenheim, R. W. Schafer, and J. R. Buck, *Discrete-Time Signal Processing*. Upper Saddle River, NJ: Prentice-Hall, 1999.
[13] E. C. Farnett and G. H. Stevens, "Pulse compression radar," in *Radar Handbook*. 2nd ed. M. Skolnik, Ed. New York: McGraw-Hill, 1990, pp. 10.1–10.39.
[14] F. J. Harris, "On the use of windows for harmonic analysis with the discrete Fourier transform," *Proc. IEEE*, vol. 66, pp. 66–67, 1978.
[15] M. A. Benkhelifa, M. Gindre, J. L. Hureou, and W. Urbach, "Echography using correlation techniques: Choice of coding signal," *IEEE Trans. Ultrason., Ferroelect., Freq. Contr.*, vol. 41, pp. 579–587, 1994.
[16] Y. C. Fung, *A First Course in Continuum Mechanics for Physical and Biological Engineers and Scientists*. 3rd ed. Engelwood Cliffs, NJ: Prentice-Hall, 1994, pp. 212–214.
[17] J. Liu, C. K. Abbey, and M. F. Insana, "Linear approach to axial resolution in elasticity imaging," *IEEE Trans. Ultrason., Ferroelect., Freq. Contr.*, vol. 51, no. 6, pp. 716–725, 2004.
[18] W. F. Walker, "The significance of correlation in ultrasound signal processing," *Proc. SPIE*, vol. 4325, pp. 159–171, 2001.
[19] T. Varghese and J. Ophir, "Performance optimization in elastography: Multicompression with temporal stretching," *Ultrason. Imag.*, vol. 18, pp. 193–214, 1996.
[20] C. Kargel, G. Plevnik, B. Trummer, and M. F. Insana, "Doppler ultrasound systems designed for tumor blood flow imaging," *IEEE Trans. Instrum. Meas.*, vol. 53, pp. 524–536, 2004.
[21] H. S. Mhanna, B. Trummer, C. Kargel, and M. F. Insana, "Ultrasonic annular array system for detecting tissue motion," *Proc. SPIE*, vol. 4687, pp. 171–181, 2002.
[22] R. J. Zemp, C. K. Abbey, and M. F. Insana, "Linear system models for ultrasonic imaging: Application to signal statistics," *IEEE Trans. Ultrason., Ferroelect., Freq. Contr.*, vol. 50, pp. 642–654, 2003.
[23] M. E. Anderson, M. S. Soo, and G. E. Trahey, "In vivo breast tissue backscatter measurements with 7.5- and 10-MHz transducers," *Ultrasound Med. Biol.*, vol. 27, pp. 75–81, 2001.
[24] L. Landini, R. Sarnelli, and F. Squartini, "Frequency-dependent attenuation in breast tissue characterization," *Ultrasound Med. Biol.*, vol. 11, pp. 599–603, 1985.
[25] R. Reghetti, S. Srinivasan, and J. Ophir, "Lateral resolution in elastography," *Ultrasound Med. Biol.*, vol. 29, pp. 695–704, 2003.

Jie Liu received her B.S. degree and M.S. degree in Biomedical Instrument from Tianjin University, Tianjin, China, in 1995 and 1997. She obtained her Ph.D. in Biomedical Engineering from the Tsinghua University, Beijing, China, in 2001. She was a Senior Research Fellow in the Bioengineering department, University of Washington, Seattle, WA, from 2001 to 2002. She has been a Postdoctoral Researcher of Biomedical Engineering at the University of California, Davis, Davis, CA, since July, 2002.

Her research interests include developing advanced scientific theories, methods, and research techniques in medical ultrasonic imaging systems and evaluating their performances in terms of diagnostic tasks.

Michael F. Insana (M'84) earned a B.S. in physics from Oakland University, Rochester, MI, in 1978 and the M.S. and Ph.D. degrees in medical physics from the University of Wisconsin, Madison, WI, in 1982 and 1983, respectively. He was a staff physicist at the Center for Devices and Radiological Health, U.S. Food and Drug Administration, Rockville, MD, from 1984–1987 working on ultrasonic tissue characterization, statistical analysis, and pattern recognition methods. From 1987–1999, Mike was professor of Radiology and Physiology at University of Kansas Medical Center, Kansas City, KS, where he conducted ultrasonics research involving the detection and progression of renal diseases.

His research activities include inverse scattering problems, elasticity imaging, biomaterials development, and observer performance experiments characterizing imaging systems. Since 1999, Mike has been Professor of Biomedical Engineering at the University of California, Davis, Davis, CA. He teaches courses on image science, signal processing, and system design and performance evaluation. Current research interests include wall-filters for strain-flow vascular imaging, elasticity imaging of breast tumors, coded-excitation approaches for B-mode, elasticity and Doppler estimation, and tissue-like phantoms. He is a member of the IEEE, the Acoustical Society of America, and a Fellow of the Institute of Physics.